GPS/LiDAR Sensor Fusion Integrity:
A Top-Down Approach

Ashwin Vivek Kanhere and Grace Xingxin Gao
University of Illinois at Urbana-Champaign

ABSTRACT

In urban environments, navigation solutions and fault detection capabilities using GPS signals are degraded due to signal blockage, non-line-of-sight reflections and multipath. These signal errors are the result of a structured environment rich in laser-based features, which provide complementary measurements to improve navigation solutions. In this work, these measurements are also used to improve navigation solution integrity and the fault detection and isolation (FDI) capabilities.

The proposed algorithm combines GPS pseudoranges with LiDAR odometry to update an Unscented Kalman Filter (UKF) navigation solution. A Receiver Autonomous Integrity Monitoring (RAIM) based framework is used to perform Fault Detection and Isolation (FDI). A heuristic for scaling LiDAR odometry covariances, for use in the FDI, is also developed.

The proposed architecture is validated with experiments conducted using data collected on the University of Illinois at Urbana-Champaign. These experiments demonstrate the effectiveness of the algorithm with and without GPS redundancy as compared to GPS-only operation.

Keywords: Sensor Fusion Integrity, LiDAR Integrity, RAIM

1 INTRODUCTION

Trustworthiness of a navigation solution is quantified by its integrity. In safety-critical applications in particular, high integrity navigation solutions are desired. For aeronautical applications, the integrity of Global Navigation Satellite System-based (GNSS-based) navigation solutions has been studied over the past three decades. One method of studying integrity: Receiver Autonomous Integrity Monitoring (RAIM) [1] [2] [3], uses redundancy in measurements to detect and isolate measurement faults. These faults may then be excluded from navigation solution calculations.

Integrity of navigation solutions obtained by using multiple GNSS constellations has been studied using the unit variance and *w*-test statistics for detection and isolation respectively [4] [5] [6]. The problem of extending GNSS only RAIM to a tightly-coupled GPS-IMU has been studied in [7] where the authors show that including the predicted filter states with pseudoranges in RAIM improves the FDI capabilities and increases the reliability of the test when compared to GPS-only RAIM.

However, in environments such as urban canyons, fewer fault-free pseudoranges are received. Tall buildings on either side of the street block signals and induce phenomena such as non-line-of-sight reflections and multipath, causing measurement faults. When these faults occur in large proportion of available GPS measurements, traditional RAIM-based FDI is severely restricted. One way to address this lack of redundancy is to use complementary sensors to aid GPS pseudoranges. In urban canyons, the large number of features present in a structured fashion makes cameras and laser-based navigation techniques ideal complements to GPS pseudoranges. This effect has been widely used to improve the quality of navigation solutions in existing literature [8]. The typical method of navigation with laser scans (for 2D, point clouds for 3D) starts by extracting features from the scan, such as lines and planes. Correspondences formed between features in consecutive scans are then used to obtain an estimate of the motion between the two consecutive scans [9].

Prior work on investigating the integrity of laser-based (LiDAR) navigation solutions has been performed in [10] where the authors performed a bottom-up study of the integrity of the navigation solution by examining the individual features. They hypothesize that major faults are caused by incorrect correspondences between features from consecutive scans. As a result, using the probability of making an incorrect data association, an independent integrity metric is calculated for the laser-based navigation solution.

In our work we explore the complementary approach, studying the integrity of laser-based navigation solutions from a top-down perspective. This paper describes a top-down laser-based navigation integrity study by a RAIM-inspired FDI algorithm that uses the GPS-LiDAR sensor fusion solution to detect faults in the combined measurement vector. This allows for redundancy

in GPS pseudoranges to be used for detecting and isolating faults in LiDAR measurements and vice versa. We consider faults as measurements that contain biases that would have otherwise been absent in an ideal scenario. We also propose a heuristic for scaling the LiDAR odometry covariance matrix to integrate LiDAR odometry and GPS pseudoranges for FDI of the combined measurement vector.

The proposed algorithm is tested using real world data to show that LiDAR odometry aids in the detection and isolation of faulty GPS pseudoranges. Additionally, results from real world data are used to show that the proposed GPS-LiDAR framework improves the integrity of the navigation solution and FDI test reliability when compared to GPS-only RAIM.

The remainder of this paper is organized as follows: Section 2 describes the proposed framework for FDI of GPS-LiDAR fusion and contains details on implementations of the UKF, FDI and LiDAR odometry covariance scaling. Section 3 contains results of experiments conducted on real world data collected on the University of Illinois at Urbana-Champaign. Finally, Section 4 concludes this paper.
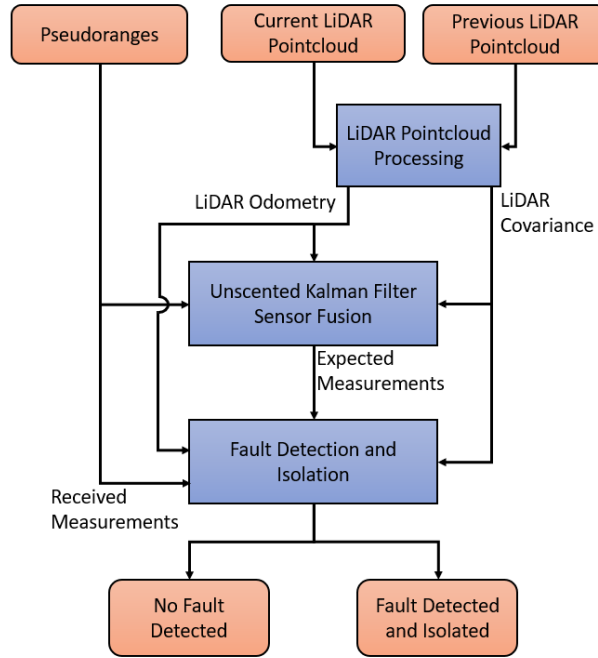

Figure 1: For the proposed algorithm, consecutive LiDAR point clouds are processed for an odometry and covariance estimate which, with the GPS pseudoranges, provides an improved navigation solution and enhanced FDI. In this figure, rectangles denote processes, ovals denote real values and rounded rectangles denote boolean values.

2   ALGORITHM

In this paper, we propose a RAIM-based framework for FDI in the combined GPS-LiDAR measurement vector. Consecutive LiDAR point clouds are processed to obtain LiDAR odometry and LiDAR odometry covariance estimates. The LiDAR odometry and covariance, along with the GPS pseudoranges, update the state estimate from the UKF-based sensor fusion. Expected measurements, obtained using the state estimate and the LiDAR odometry covariance are used in for FDI of the combined received measurement vector. The output of the proposed algorithm indicates whether no fault was detected in the measurement vector, or a fault was detected and isolated.

The scaling of the LiDAR odometry covariance [11] is crucial before integration of the LiDAR odometry with the GPS pseudoranges in the FDI step. A detailed description of the heuristic used to scale the LiDAR odometry covariance for this purpose is given in Section 2.3. A schematic of the proposed algorithm, as described above, is shown in Figure 1.

2.1   Unscented Kalman Filter (UKF)

An improved estimate of the navigation states augments the algorithm's FDI performance. For this purpose, all available measurements are used in an UKF-based sensor fusion [12] [13] to obtain a position estimate. A schematic of the UKF used in
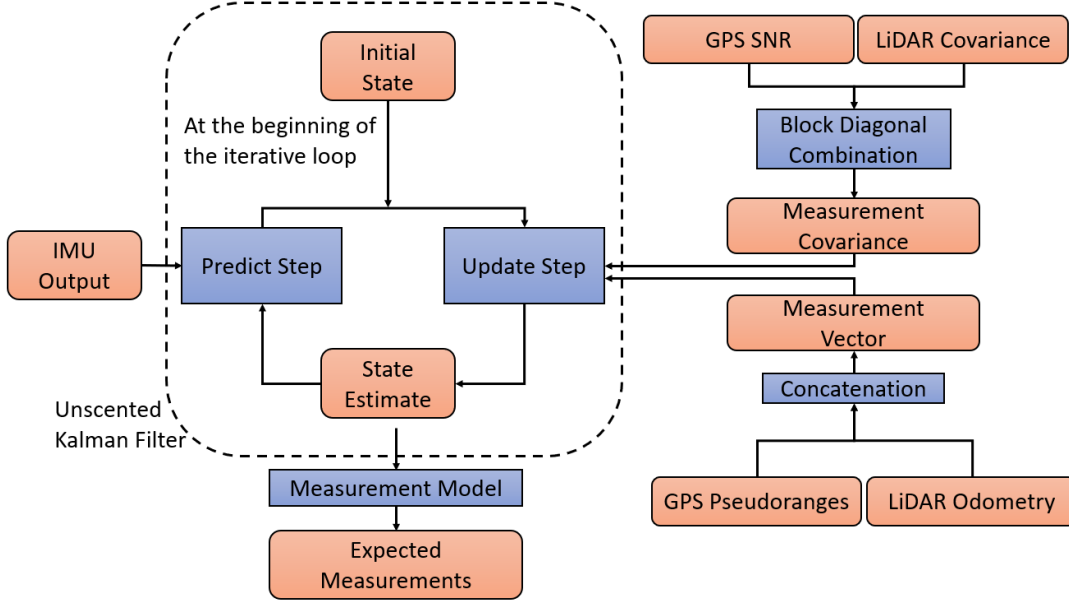
Figure 2: Schematic of the UKF used in the algorithm. IMU measurements are used for the state estimate propagation. Using a combined measurement of the LiDAR odometry and GPS pseudoranges with measurement dependent covariance matrices increases the filter performance. In this figure, ovals denote real values and rectangles denote functions and processes.

this work is given in Figure 2. A detailed mathematical description of the UKF equations can be found in [14].

The state vector X estimated by the UKF, is defined as:

$$X = \begin{bmatrix} x_n & v_n & q_n^b & b_a & b_g & b_c \end{bmatrix}^T \tag{1}$$

where x_n is the position in the local North-East-Down (NED) frame of reference, v_n is the velocity in this NED navigation frame, q_n^b is the quaternion estimate of the orientation of the body frame with respect to the NED frame of reference, b_a and b_g are estimates of the accelerometer and gyroscope biases respectively and b_c is the estimate of the receiver clock bias. The orientation states are estimated for a future version of this work, where the LiDAR odometry will be used to update the body orientation.

The UKF is initialized in an open-sky environment which yields a low-uncertainty Earth Centred Earth Fixed (ECEF) position estimate and an estimate of the receiver clock bias. The ECEF position estimate is used to define a local NED navigation frame of reference for the rest of the trajectory, with the initial position as the origin for this NED frame. Since the distances in this particular application are short, it is assumed that the navigation frame is the same throughout the trajectory.

The origin of the NED and the initial estimate of the receiver clock bias are used to initialize the UKF. The orientation of the body is initialized by aligning the IMU frame of reference to the local NED frame of reference [15] while the velocities and acceleration and gyroscopic biases are initialized as 0.

A constant velocity dynamic model is used for the propagation model in the filter. The model is described in Eq. 2 and has been adapted from [16].

$$\dot{X} = \begin{bmatrix} \dot{x}_n \\ \dot{v}_n \\ \dot{q}_n^b \\ \dot{b}_a \\ \dot{b}_g \\ \dot{b}_c \end{bmatrix} = \begin{bmatrix} v_n \\ -R_{q_n^b} b_a - g \\ \frac{-1}{2}\Gamma_{q_n^b} b_g \\ 0 \\ 0 \\ 0 \end{bmatrix} + \begin{bmatrix} 0 \\ 0 \\ \frac{1}{2}\Gamma_{q_n^b} \\ 0 \\ 0 \\ 0 \end{bmatrix} \omega_b + \begin{bmatrix} 0 \\ R_{q_n^b} \\ 0 \\ 0 \\ 0 \\ 0 \end{bmatrix} a_b \tag{2}$$

Here $R_{q_n^b}$ is the equivalent rotation matrix for the quaternion estimate q_n^b and $\Gamma_{q_n^b}$ is the quaternion rate of change matrix[15]. The Inertial Measurement Unit (IMU) measurements of body accelerations (a_b) and body angular velocities (ω_b) are used for state propagation. The process covariance matrix Q is manually tuned to maximize filter performance.

At every iteration of the filter, the update step is used to correct the propagated state estimates. The measurement vector z is computed using the measurement model:

$$z = \begin{bmatrix} \Delta\hat{x}_{LiDAR} & \Delta\hat{y}_{LiDAR} & \Delta\hat{z}_{LiDAR} & \hat{\rho}^1 & \hat{\rho}^2 & \dots & \hat{\rho}^k \end{bmatrix}^T \tag{3}$$

where $\begin{bmatrix} \Delta\hat{x}_{LiDAR} & \Delta\hat{y}_{LiDAR} & \Delta\hat{z}_{LiDAR} \end{bmatrix}^T$ is the LiDAR odometry in the NED frame of reference and $\hat{\rho}^1, \dots, \hat{\rho}^k$ are the k received pseudoranges.

The measurement model used to update the filter is defined in two parts: the pseudorange model is given in Eq. 4 and the LiDAR odometry model is given in Eq. 5. The measurement model yields the expected measurements, which are an estimate of the received measurements at the propagated state estimate. Intuitively, the UKF updates the propagated state estimate with a covariance-weighted difference between the expected measurements and received measurements.

The pseudorange measurement model accounts for satellite and receiver clock offsets and tropospheric and ionospheric delays and can be further explored in [17]. This pseudorange measurement model is:

$$\hat{\rho}^k = r^k + \left(b_c - \delta t^k\right) + I^k + T^k + \epsilon^k \tag{4}$$

where r^k is the true range between the receiver and satellite, b_c is the receiver clock bias estimate, δt^k is the satellite clock delay, I^k is the ionospheric delay, T^k is the tropospheric delay and ϵ^k is the error between the estimated and real pseudoranges. ϵ^k is modelled as a zero-mean Gaussian random variable [1].

The LiDAR measurement model giving the expected measurements for the propagated state, is as follows:

$$\begin{bmatrix} \Delta\hat{x}_{LiDAR} \\ \Delta\hat{y}_{LiDAR} \\ \Delta\hat{z}_{LiDAR} \end{bmatrix} = \begin{bmatrix} x_{current} - x_{previous} \\ y_{current} - y_{previous} \\ z_{current} - z_{previous} \end{bmatrix} \tag{5}$$

where $x_{previous}$ is the NED position along the x-axis when the last LiDAR odometry measurement was received and $x_{current}$ is the current state estimate. This similarly extends to $\Delta\hat{y}_{LiDAR}$ and $\Delta\hat{z}_{LiDAR}$ for the y-axis and z-axis odometry respectively. The LiDAR odometry is obtained by performing Iterative Closest Points (ICP) between consecutive point clouds to obtain a 3D affine transformation matrix. This affine transformation matrix is then further processed to obtain the distance travelled in the NED frame of reference, which is passed to the filter as the LiDAR odometry vector.

The measurement covariance matrix $\left(R_{UKF} \in \mathbb{R}^{k+3 \times k+3}\right)$ is obtained by combining an estimate of the LiDAR odometry covariance $\left(R_{LiDAR} \in \mathbb{R}^{3 \times 3}\right)$ [11] and a SNR based covariance for the GPS pseudoranges [18] of the form:

$$R_{GPS} = \mathrm{diag}\left[10^{-\frac{SNR_1}{10}}, 10^{-\frac{SNR_2}{10}}, \dots 10^{-\frac{SNR_k}{10}}\right] \tag{6}$$

where R_{GPS} is a diagonal matrix $\in \mathbb{R}^{n \times n}$.

LiDAR odometry and GPS pseudoranges are manually tuned by scaling their values of relative to each other. This yields the measurement covariance matrix given in Eq. 7:

$$R_{UKF} = \begin{bmatrix} \mu_{LiDAR} R_{LiDAR} & 0 \\ 0 & \mu_{GPS} R_{GPS} \end{bmatrix} \tag{7}$$

Here, μ_{LiDAR} and μ_{GPS} are the tuning factors for the LiDAR odometry covariance and GPS measurement covariance respectively. These tuning parameters are manually tuned to maximize filter performance.

At the end of every iteration the state estimate is used with the measurement model to obtain the expected measurements, which are passed which are passed with the LiDAR odometry covariance estimate for FDI.

2.2 Fault Detection and Isolation (FDI)

The expected measurements and the LiDAR covariance are used for the FDI in the received measurements. An overall schematic of this algorithm is shown in Figure 3. To integrate the LiDAR odometry and pseudorange measurements, the LiDAR odometry covariance estimate must be scaled absolutely with respect to the LiDAR odometry residual, which is discussed further in Section 2.3.

The expected and received measurements are differenced to give the measurement residual which is used with the combined measurement covariance to calculate the value of the detection statistic. The unit variance test [4], given in Eq. 8, is used as the detection statistic:

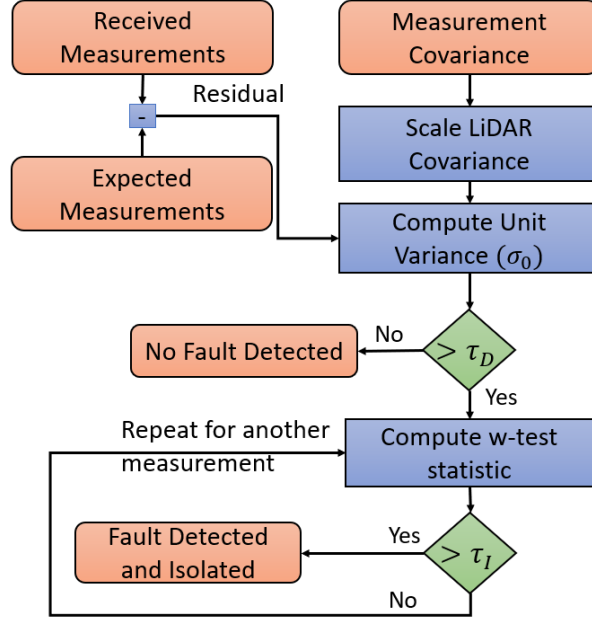$$\sigma_0^2 = \frac{v^T R^{-1} v}{n - m} \tag{8}$$

Figure 3: The received and expected measurements are differenced to yield a measurement residual. Scaling the LiDAR odometry covariance for integration into the measurement covariance matrix lets us perform FDI on the combined received measurement vector. In this figure, ovals denote real values, rounded triangles denote boolean values, rectangles denote processes and diamonds denote value comparisons.

Here, v is the measurement residual vector, R is the combined measurement covariance matrix, n is the number of received measurements and m is the number of unknowns.

For FDI the combined measurement covariance matrix is:

$$R = \begin{bmatrix} \bar{R}_{LiDAR} & 0 \\ 0 & \sigma\left(\epsilon^k\right)^2 I_k \end{bmatrix} \tag{9}$$

Here, $I_k \in \mathbb{R}^{k \times k}$ is the identity matrix and the pseudorange error standard deviation $\sigma\left(\epsilon^k\right) = 5$ is used [1]. Details on the heuristic for obtaining $\bar{R}_{LiDAR}$ are given in Section 2.3.

For the proposed framework, $n = k + 3$, where k is the number of received pseudoranges and there are 3 LiDAR odometry measurements. There are 4 unknowns $[x, y, z, b_c]$, where x, y and z are the unknown positions and b_c, the receiver clock bias, giving $m = 4$.

The threshold value τ_D is given as:

$$\tau_D = \chi^2_{1-\alpha, n-m} \tag{10}$$

where α is the probability of false alarm as given by the integrity requirement. If $\sigma_0^2 > \tau_D$ a fault is detected and fault isolation is performed. If the value of σ_0^2 is below τ_D, no fault is detected.

For the fault isolation part of the algorithm the w-test statistic [7], a vector of values corresponding to each measurement, is used. For the fault isolation, the measurement with the largest value of w_i, exceeding the threshold, is selected as the candidate fault. The unit variance test is calculated without this measurement. If the new calculated unit variance test is below the threshold τ_D, the faulty measurement has been isolated. This procedure is repeated until the measurement fault is isolated. The threshold for the w-test statistic is $\tau_I = Q^{-1}\left(1 - \alpha\right)$ where Q is the cumulative distribution function for the standard normal distribution.

The w-test statistic for fault isolation has been applied to a least squares-based solution in previous work [7]. In this paper, we assume that the UKF provides an estimate of the optimal least squares solution which allows us to adapt the w-test statistic from [7] for the GPS-LiDAR FDI framework. The estimate for the optimal Kalman gain is given in Eq. 11:

$$\hat{K} = \left(A^T R^{-1} A\right)^{-1} \tag{11}$$

where A is the matrix for the linearized measurement model: $z = Ax$. This measurement model is an approximation of the model described in Eq. 3.

An estimate of the residual cofactor matrix is given in Eq. 12:

$$\hat{V} = R^{-1} - A\hat{K}A^T \tag{12}$$

The w-test statistic vector is calculated by finding w_i for each measurement as given in Eq. 13:

$$w_i = \left| \frac{e_i^T R^{-1} \hat{v}}{\sqrt{e_i^T R^{-1} \hat{V} R^{-1} e_i}} \right| \tag{13}$$

Here, e_i is a $\mathbb{R}^n$ vector where the ith component is 1 and all other components are 0. R is the measurement covariance matrix obtained by combining the scaled LiDAR odometry covariance and GPS pseudorange error model.

2.3 LiDAR Covariance Scaling

The LiDAR odometry covariance estimate is used in both the UKF and FDI steps of the algorithm. This covariance is obtained by the algorithm described in [11]. This LiDAR odometry covariance estimate quantifies the relative uncertainty in the odometry along a particular axis with respect to the other axes of the odometry. While this covariance is tuned manually for the UKF, for use in FDI the covariance estimate must be absolutely scaled to the residual vector of the LiDAR odometry. While doing so, it is desired that information of the relative uncertainty along individual axes is maintained as well. This is performed using the heuristic method outlined in the following steps:

1. Obtain an estimate for the distance D travelled in a single time instant in the odometry by calculating the L_2 norm of the received LiDAR odometry measurement. D is used to scale the LiDAR covariance matrix estimate.

2. Normalize the covariance matrix by dividing it by $|R_{LiDAR}|^{1/3}$. This will ensure that the determinant of the normalized covariance matrix is 1.

3. Scale the LiDAR odometry covariance by multiplying the normalized covariance matrix obtained in step 2 by the scaling factor obtained in step 1.

For the unscaled LiDAR covariance estimate, R_{LiDAR}, the scaled LiDAR covariance estimate $\bar{R}_{LiDAR}$ is given by:

$$\bar{R}_{LiDAR} = D \frac{R_{LiDAR}}{|R_{LiDAR}|^{1/3}} \tag{14}$$

The scaled LiDAR covariance matrix is then combined with a static estimate of the pseudorange errors to form the measurement covariance matrix R as described in Eq. 9.

The choice of the unit variance and w-test statistics allows the FDI framework to fully utilize the all the complete information present in the measurement covariance matrix. Coupled with the preservation of relative scale by the scaling heuristic, this extends the FDI to individual odometry axes.

2.4 Test Reliability and Residual Separability

The change in reliability of the GPS-LiDAR fusion RAIM and GPS-only RAIM is ascertained by comparing the Minimal Detectable Biases (MDBs) for individual GPS measurements for both cases. Described in more detail in [5], the MDBs were calculated for each measurement using Eq. 15:

$$MDB_i = \frac{\delta_0}{\sqrt{e_i^T R^{-1} \hat{V} R^{-1} e_i}} \tag{15}$$

Here, δ_0 is the non-centrality parameter and is determined by the values of α and γ (the detectability of the test). For this implementation, the value of $\delta_0 = 2.8$ [7].

Intuitively, MDBs quantify the minimum bias in measurements that are detected by the test statistics given α and γ. Both α and γ are specified in the integrity requirements and are known to us. Lower MDBs indicate that the test is more effective at
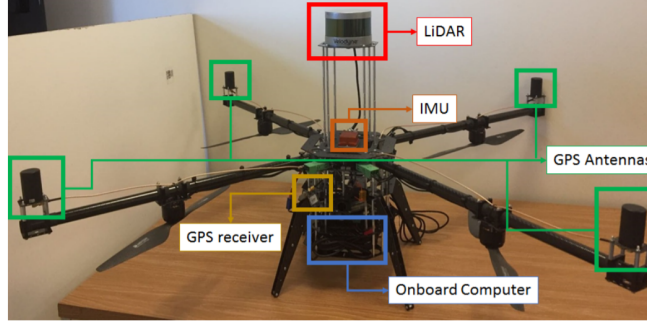
Figure 4: iBQR v1 with the data collection setup.

detecting biased residuals and is, hence, performing better.

Additionally, the separability of the different components of the residual vectors is also calculated. Given by the matrix $[\nu_{ij}]$, each value of the matrix denotes the ease of isolation of faults in individual measurements. The value of ν_{ij} varies between 0 and 1, where a smaller value indicates easier isolation of faults while a higher value indicates that even after a fault is detected, it is hard to isolate the individual measurement causing the fault. Described in more detail in [4], Eq. 16 is used to calculate the value for ν_{ij}:

$$\nu_{ij} = \frac{e_i^T R^{-1} \hat{V} R^{-1} e_j}{\sqrt{e_i^T R^{-1} \hat{V} R^{-1} e_i} \sqrt{e_j^T R^{-1} \hat{V} R^{-1} e_j}} \tag{16}$$

3 EXPERIMENTATION

To validate the algorithm proposed in Section 2, experiments were performed using data collected on the University of Illinois at Urbana-Champaign campus. The data was collected using our custom quadcopter platform, the Illinois Big Quadrotor (iBQR) v1. Our sensor suite comprised of a Velodyne VLP-16 Puck Lite LiDAR, a ublox LEA-6T GPS receiver connected to a Maxtena antenna, and an Xsens MTi-30 IMU. These were used to collect the LiDAR point clouds, GPS pseudoranges and body accelerations and angular velocities respectively. We used an AscTec MasterMind as the on-board computer for sensor data logging. The data collection setup is shown in Figure 4.

The GPS-LiDAR framework was tested on data that was collected for a duration of 150s on a trajectory starting from the entrance to the Coordinated Science Laboratory building and ending on the West wall of the Beckman Institute, covering a distance of 55m × 130m.

The LiDAR return range was restricted to 15m to simulate operating conditions where the required feature density for sufficiently accurate odometry estimation is lacking. During the entire trajectory, 8-10 GPS satellites are visible. A few measurements have relatively high residuals with respect to the navigation solution. Some GPS satellites also have intermittently fluctuating visibility during the trajectory.

3.1 Sensor Fusion Results

The navigation solutions calculated using individual sensors independently have shortcomings. The LiDAR odometry navigation solution shows a drift that increases with the progress of time and the GPS Newton-Raphson navigation solution shows poor position tracking throughout the entire trajectory. The GPS-LiDAR sensor fusion navigation solution yields a superior navigation solution by leveraging the complementary nature of GPS and LiDAR measurements. Figure 5 depicts a plot of the sensor fusion results along with the recorded ground truth for the selected trajectory.

3.2 FDI without Redundancy of GPS Measurements

To verify that the proposed framework detects faults in received measurements, a measurement vector comprising of the LiDAR odometry and 4 high elevation GPS satellite measurements was considered for the first 70 s of the collected data. Of these 4 GPS pseudoranges, a bias of 100m was injected in one pseudorange for the first 30 s. The variation of the resultant fault detection statistic with resepect to the fault detection threshold is shown in Figure 6.
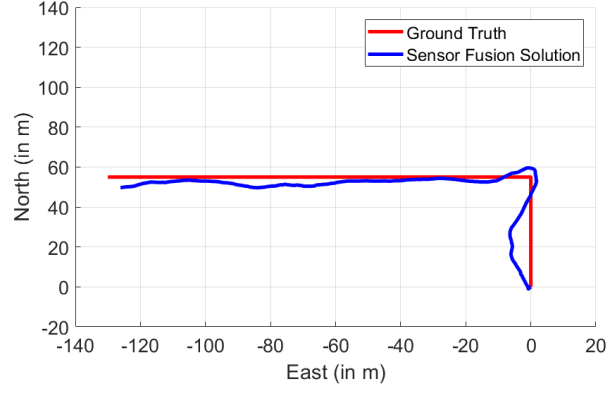
Figure 5: GPS-LiDAR sensor fusion based navigation solution. The average position error in the NED frame is reduced to 6m from an error of 21m in the LiDAR odometry and 80m GPS Newton Raphson solution.
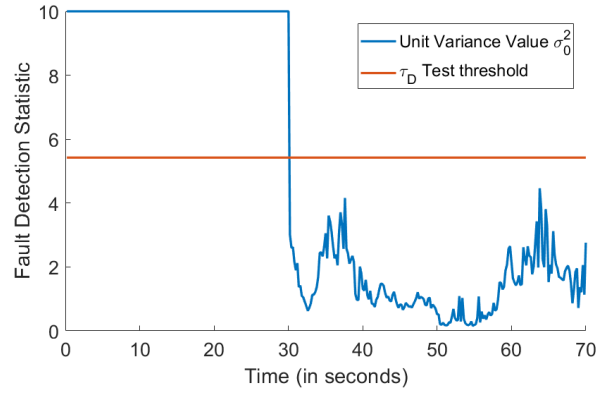

Figure 6: Variation of unit variance statistic σ_0^2 and the detection threshold τ_D with time. A fault is correctly identified for the 0s-30s when a pseudorange bias is added. The absence of a fault is also correctly identified for the 30s-70s range, when no pseudorange bias is added.
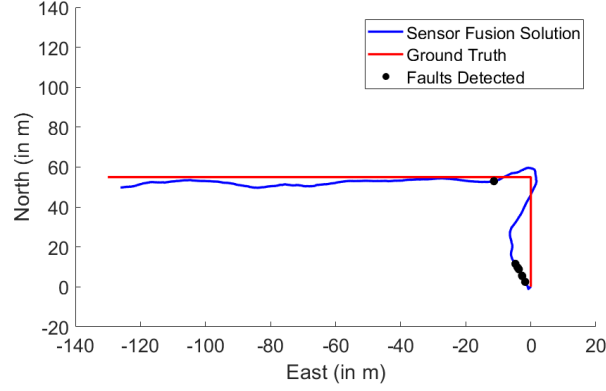
Figure 7: Instances at which faults were detected in the sensor fusion solution using the proposed framework are shown as black scatter points on the sensor fusion solution with the ground truth for reference.

The injected fault was detected and isolated in all cases. The graph in Figure 6 shows that the value for σ_0^2 is above the threshold τ_D when a bias is injected and below τ_D when the bias is no longer injected. This demonstrates that our proposed algorithm effectively detects existing measurement faults along with maintaining a low false alarm rate.

3.3 Comparison of GPS-LiDAR fusion FDI to GPS-only FDI

These experiments were conducted using the full 150s of collected data. Fault detection was performed for the measurement vector consisting of pseudoragnes from all visible satellites and the LiDAR odometry vector. This implementation of our proposed framework was compared to a GPS-only RAIM framework with the same integrity requirements.

The proposed GPS-LiDAR framework improves performance when compared to a GPS-only RAIM in two ways: improving the navigation solution and providing additional measurement redundancy. The added measurement redundancy supporting the obtained navigation solution improves its integrity while ensuring better FDI performance.

The UKF-based navigation solution was used for the proposed GPS-LIDAR FDI framework and the GPS Newton Raphson solution was used for GPS-only RAIM. Out of the 759 measurement instances, faults were detected in 324 instances by the GPS-only RAIM solution. The GPS-LiDAR fusion RAIM detected faults in only 7 out of 759 instances. Fewer detected faults with similar frameworks and integrity requirements signifies that the better solution is supported by the measurement redundancy, indicating an improvement in navigation integrity.

This shows that our proposed framework improves the navigation solution coupled with an increase the integrity of the navigation solution. The instances at which faults were detected are shown in Figure 7. The GPS-challenged environment in which the data was collected causes a high number of measurement faults to be detected by both FDI tests. These faults are caused by multipath and NLOS reflections of the GPS signals received by the antenna. The percentage change in the MDBs of the pseudoranges is also calculated for the GPS-LiDAR fusion FDI when compared to the GPS-only FDI. The pseudorange MDBs show a decrease for all PRNs, with large decreases for some particular PRNs. This shows that the reliability of the test increases when using the GPS-LiDAR fusion FDI framework as opposed to a GPS-only FDI framework. The average percentage change in MDBs is shown in Figure 8.

Additionally, the separability of the measurements between LiDAR odometry measurements and GPS pseudoranges was calculated. These measurements can be consistently isolated which is supported by the consistently low value of the relevant ν_{ij}.

4 CONCLUSIONS

In this work, we proposed a FDI framework for GPS-LiDAR sensor fusion utilizing RAIM. LiDAR odometry was integrated with the GPS pseudoranges by scaling the LiDAR covariance matrix for a top-down study of LiDAR measurement integrity. Experiments were conducted using real world data collected on the University of Illinois at Urbana-Champaign campus to show that the proposed algorithm successfully detected and isolated faulty pseudoranges in a situation without redundant GPS pseudoranges. Experiments also showed that the navigation solution obtained by the proposed framework had higher integrity
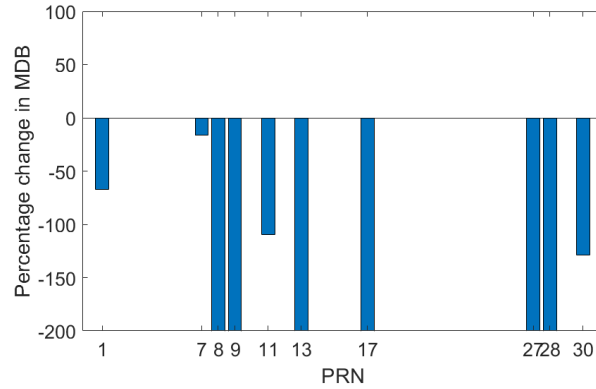
Figure 8: Time-Averaged Percentage Change in pseudorange MDBs on using GPS-LiDAR FDI when compared to GPS-only FDI. The reduced MDBs show that the reliability of the GPS-LiDAR FDI test is greater than the GPS-only FDI test.

when compared to a GPS-only navigation solution and that the reliability of the FDI test increased on using the proposed GPS-LiDAR framework.

5 ACKNOWLEDGEMENTS

REFERENCES

[1] B. W. Parkinson and P. Axelrad, "Autonomous gps integrity monitoring using the pseudorange residual," *Navigation*, vol. 35, no. 2, pp. 255–274, 1988.

[2] R. G. Brown, "Receiver autonomous integrity monitoring," *Global Positioning System: Theory and applications.*, vol. 2, pp. 143–165, 1996.

[3] M. Joerger, F.-C. Chan, and B. Pervan, "Solution separation versus residual-based raim," *Navigation: Journal of The Institute of Navigation*, vol. 61, no. 4, pp. 273–291, 2014.

[4] S. Hewitson, H. K. Lee, and J. Wang, "Localizability analysis for gps/galileo receiver autonomous integrity monitoring," *The journal of Navigation*, vol. 57, no. 2, pp. 245–259, 2004.

[5] S. Hewitson and J. Wang, "Gnss receiver autonomous integrity monitoring (raim) performance analysis," *Gps Solutions*, vol. 10, no. 3, pp. 155–170, 2006.

[6] ——, "Gnss receiver autonomous integrity monitoring with a dynamic model," *The Journal of Navigation*, vol. 60, no. 2, pp. 247–263, 2007.

[7] ——, "Extended receiver autonomous integrity monitoring (e raim) for gnss-ins integration," *Journal of Surveying Engineering*, vol. 136, no. 1, pp. 13–22, 2010.

[8] A. Soloviev, "Tight coupling of gps, laser scanner, and inertial measurements for navigation in urban environments," in *Position, Location and Navigation Symposium, 2008 IEEE/ION*. IEEE, 2008, pp. 511–525.

[9] J. Zhang and S. Singh, "Loam: Lidar odometry and mapping in real-time." in *Robotics: Science and Systems*, vol. 2, 2014, p. 9.

[10] M. Joerger, M. Jamoom, M. Spenko, and B. Pervan, "Integrity of laser-based feature extraction and data association," in *Position, Location and Navigation Symposium (PLANS), 2016 IEEE/ION*. IEEE, 2016, pp. 557–571.

[11] A. Shetty and G. X. Gao, "Covariance estimation for gps-lidar sensor fusion for uavs," in *Proceedings of the 30th International Technical Meeting of The Satellite Division of the Institute of Navigation (ION GNSS+ 2017), Portland, OR, USA*, 2017.

[12] E. A. Wan and R. Van Der Merwe, "The unscented kalman filter for nonlinear estimation," in *Adaptive Systems for Signal Processing, Communications, and Control Symposium 2000. AS-SPCC. The IEEE 2000*.   IEEE, 2000, pp. 153–158.

[13] Y. Li, C. Rizos, J. Wang, P. Mumford, and W. Ding, "Sigma-point kalman filtering for tightly coupled gps/ins integration," *Navigation*, vol. 55, no. 3, pp. 167–177, 2008.

[14] R. Van Der Merwe, E. A. Wan *et al.*, "Sigma-point kalman filters for integrated navigation," in *Proceedings of the 60th Annual Meeting of the Institute of Navigation (ION)*, 2004, pp. 641–654.

[15] D. Titterton, J. L. Weston, and J. Weston, *Strapdown inertial navigation technology*.   IET, 2004, vol. 17.

[16] J. Kelly and G. S. Sukhatme, "Visual-inertial sensor fusion: Localization, mapping and sensor-to-sensor self-calibration," *The International Journal of Robotics Research*, vol. 30, no. 1, pp. 56–79, 2011.

[17] P. Misra and P. Enge, "Global positioning system: signals, measurements and performance (second edition)," *Massachusetts: Ganga-Jamuna Press*, 2006.

[18] J. Collins and R. Langley, "Possible weighting schemes for gps carrier phase observations in the presence of multipath," *Final contract report for the US Army Corps of Engineers Topographic Engineering Center, No. DAAH04-96-C-0086/TCN*, vol. 98151, 1999.

BIOGRAPHIES

Ashwin Vivek Kanhere received his B.Tech degree in Aerospace Engineering with a minor in Electrical Engineering from the Indian Institute of Technology Bombay, Mumbai in 2017. He is currently a graduate student in the department of Aerospace Engineering at the University of Illinois at Urbana-Champaign.

Grace Xingxin Gao received the B.S. degree in Mechanical Engineering and the M.S. degree in electrical engineering from Tsinghua University, Beijing, China in 2001 and 2003. She received the PhD degree in Electrical Engineering from Stanford University in 2008. From 2008 to 2012, she was a research associate at Stanford University. Since 2012, she has been with University of Illinois at Urbana-Champaign, where she is presently an assistant professor in the Aerospace Engineering Department.